Available online at www.sciencedirect.com
ScienceDirect
Surface Science 600 (2006) 5041–5050
SURFACE SCIENCE
www.elsevier.com/locate/susc

In situ gas-phase catalytic properties of TiC-supported size-selected gold nanoparticles synthesized by diblock copolymer encapsulation

L.K. Ono [a], D. Sudfeld [b], B. Roldan Cuenya [a,*]

[a] Department of Physics, University of Central Florida, Orlando, FL 32816, United States
[b] Department of Physics, University of Duisburg-Essen, D-47048, Duisburg, Germany

Received 5 June 2006; accepted for publication 21 August 2006
Available online 12 September 2006

Abstract

TiC-supported size- and shape-selected Au nanoparticles with well defined interparticle distances were synthesized by diblock copolymer encapsulation. Atomic force microscopy (AFM), transmission electron microscopy (TEM), X-ray photoelectron spectroscopy (XPS) and temperature programmed desorption (TPD) have been used to investigate the correlation between the nanocatalyst morphological/electronic structure and its chemical reactivity. Using the low-temperature oxidation of CO as a model reaction, our TPD results showed an enhancement of the catalytic activity with decreasing particle size. Two desorption features were observed and assigned to kinks/steps in the gold surface and the Au–TiC interface. The role of the interparticle distance on the activity is discussed. AFM measurements showed drastic morphological changes (Ostwald ripening) on the nanoparticles after CO oxidation when the initial interparticle distance was small (~30 nm). However, no sintering was observed for Au nanoparticles more widely spaced (~80 nm).

Keywords: Catalysis; Gold nanoparticle; Titanium carbide; Carbon monoxide; Oxygen; Diblock copolymer; Thermal desorption spectroscopy; Atomic force microscopy (AFM); X-ray photoelectron spectroscopy (XPS); Transmission electron microscopy (TEM); Surface structure, morphology, roughness, and topography

1. Introduction

Until the beginning of the 80s, gold was considered a poor candidate for heterogeneous catalysis applications, since reactive gases like O_2 do not adsorb on bulk gold surfaces [1]. Extensive studies conducted by Bond et al. [2] showed the unusual catalytic performance of small gold particles supported on silica for highly selective hydrogenation reactions. Later on, Haruta et al. [3] demonstrated the dramatic enhancement of the catalytic activity and selectivity of highly dispersed gold particles (<5 nm) supported on reducible metal oxides for a number of reactions including CO oxidation, combustion of hydrocarbons and reduction of nitrogen oxides [4]. This work also drew attention to the influence of the nanoparticle preparation method on the catalyst's performance. ''Coprecipitated'' Au nanoparticles were found to be more active than ''impregnated'' nanocatalysts for low-temperature CO oxidation [5]. In the last 25 years, researchers have found that gold nanoparticles are excellent catalysts for many other technological and environmentally important reactions such as hydrogenation of CO_2 and CO into methanol and decomposition of halogenated compounds [4].

Since the first experimental observations, considerable efforts have been dedicated to the systematic investigation of the influence of nanoparticle size [4–9], shape [4], and nanoparticle–metal-oxide support interaction [4,10] on the catalytic activity [11].

One of the most broadly studied catalytic reactions is the low-temperature oxidation of CO. Despite the large amount of published work available, the origin of the unusual catalytic properties of supported metallic nanoparticles is still under discussion. Having as a common goal

* Corresponding author. Tel.: +1 407 823 1883; fax: +1 407 823 5112.
E-mail address: roldan@physics.ucf.edu (B. Roldan Cuenya).

0039-6028/$ - see front matter © 2006 Elsevier B.V. All rights reserved.
doi:10.1016/j.susc.2006.08.025

the understanding of catalysis at the atomic level, previous researchers proposed different models that could explain the high activity of small metallic nanoparticles [5,12–15]. Goodman's group suggested that the high activity of small gold particles is related to quantum-size effects generated by electrons confined within a small volume [6,16]. Based on scanning tunneling spectroscopy (STS) studies, a size-dependent metal-to-semiconductor transition was observed, and a correlation between the appearance of a band gap and catalytic activity established. In addition, they observed that bi-layer structure showed higher activity compared to monolayer structure [13,17]. However, recent density functional theory (DFT) calculations by Mills et al. [18] showed that the presence of a band gap might not be essential to the chemical activity of a cluster. Temperature programmed desorption (TPD) studies of CO desorption from different Au coverages deposited on FeO(1 1 1) carried out by Freund et al. [19] indicated that the reactivity of gold nanoparticles arises from the presence of highly uncoordinated gold atoms instead of quantum-size effects. Based on DFT calculations on gold surfaces, Mavrikakis et al. [15,20] found that CO, O and O_2 preferentially chemisorb on stepped surfaces. The authors concluded that the enhanced reactivity of small particles could be related to their high step densities. This is in agreement with previous experimental observations by Yates and coworkers [21,22]. Also it has been long accepted that the roughness play a vital role in the catalysis surfaces [23–25].

Haruta et al. [5] suggested that the catalytic activity of gold nanoparticles for CO oxidation depends strongly on the nanoparticle/support contact area, i.e., on the particle's shape. Different preparation methods yield different shapes, and hemispherical particles were found to perform better than spherical particles. These results also indicated that the catalytic reactions may occur at the perimeter interfaces around the Au particles, where the fraction of step sites increases significantly with decreasing particle size [5]. Hakkinen et al. [26] attributed the enhanced catalytic properties of small gold nanoparticles to charge transfer from the metal-oxide support to the nanoparticle surface. However, a recent review article by Lopez et al. [15] that compiled available experimental data on CO oxidation by gold concluded that the particle size (and not the support) was the determining factor controlling the catalyst's performance. Charge transfer from oxygen vacancies in the support to the gold particles as well as the interaction of adsorbates with the nanoparticle-support perimeter surfaces were found not to significantly contribute to the observed activity. The authors pointed out that the density of low-coordinate sites affects strongly the chemical activity and concluded that the activity follows a scaling law of $\sim 1/d^3$, with d being the particle diameter.

A non-monotonic size-dependent resistance towards oxidation was reported by Boyen et al. [27], where closed-shell Au_{55} clusters (1.4 nm) encapsulated on $(PPh3)_{12}Cl_6$ were found to remain inert under strong oxidizing conditions. Later on, investigations by Roldan et al. [7,8] suggested that the ability of certain cluster sizes to stabilize larger amounts of Au^{3+} upon O_2-plasma exposure could be related to the enhanced catalytic performance of those particular particle sizes for CO electro-oxidation. The influence of the oxidation state of gold on its reactivity for CO oxidation is still under debate [28,29].

The present paper investigates the influence of particle size and shape on the chemical reactivity of gold. The low-temperature oxidation of CO on gold nanoparticles of sizes ranging from 2 nm to 6 nm supported on thin TiC films is used as a model reaction system. Transition metal carbides such as WC and MoC are known to exhibit reactivities similar to Pt-based catalysts for dehydrogenation, hydrogenolysis and isomerization reactions [30–33]. The catalytic properties of TiC for reactions involving water, SO_2 [34], ethanol [35,36] and methanol [37] have been investigated in the past. For example, Chen et al. observed that ~70% of adsorbed water in the first monolayer reacts with TiC producing CO and H_2 [35]. Kojima et al. observed that TiC catalyzes the hydrogenation of CO to produce methane and higher molecular weight hydrocarbons [38,39]. To the best of our knowledge, there are no CO oxidation studies on TiC substrates in the literature.

The gold nanoparticles under investigation were synthesized by diblock copolymer encapsulation. This is a well-established method that results in nanoparticles with very narrow size distributions hexagonally arranged on the desired substrate [40]. Information on the nanoparticle structure, size and dispersion were obtained by high-resolution transmission electron microscopy (HR-TEM) and atomic force microscopy (AFM). Details on the nanoparticle and support chemical compositions were obtained by X-ray photoelectron spectroscopy (XPS), and insight into their catalytic activity was obtained by TPD. The following study will show that pure TiC is inactive for CO oxidation at low temperature. However, size-dependent catalytic activity is observed when gold nanoparticles are dispersed on ultrathin TiC films.

2. Experimental section

Size- and shape-selected gold nanoparticles with narrow size distributions have been synthesized by inverse micelle encapsulation [41]. A detailed description of the preparation method used can be found in Refs. [7,8]. Nanoparticles of different sizes and interparticle distances were synthesized using commercially available diblock copolymers, polystyrene-block-poly(2-vynilpyridine) (PS(x)-b-P[2VP](y), Polymer Source Inc.) as encapsulating agents, chloroauric acid ($HAuCl_4 \cdot 3H_2O$) as metal seed, and toluene as solvent. Keeping constant the concentration of $HAuCl_4$, the nanoparticle size and interparticle distance can be tuned by changing the length of the diblock copolymer head (P2VP) and tail (PS), respectively (see Fig. 1). Further control over the nanoparticle size can be gained by changing the relative concentration of $HAuCl_4$ versus P2VP ($r = HAuCl_4$ P2VP

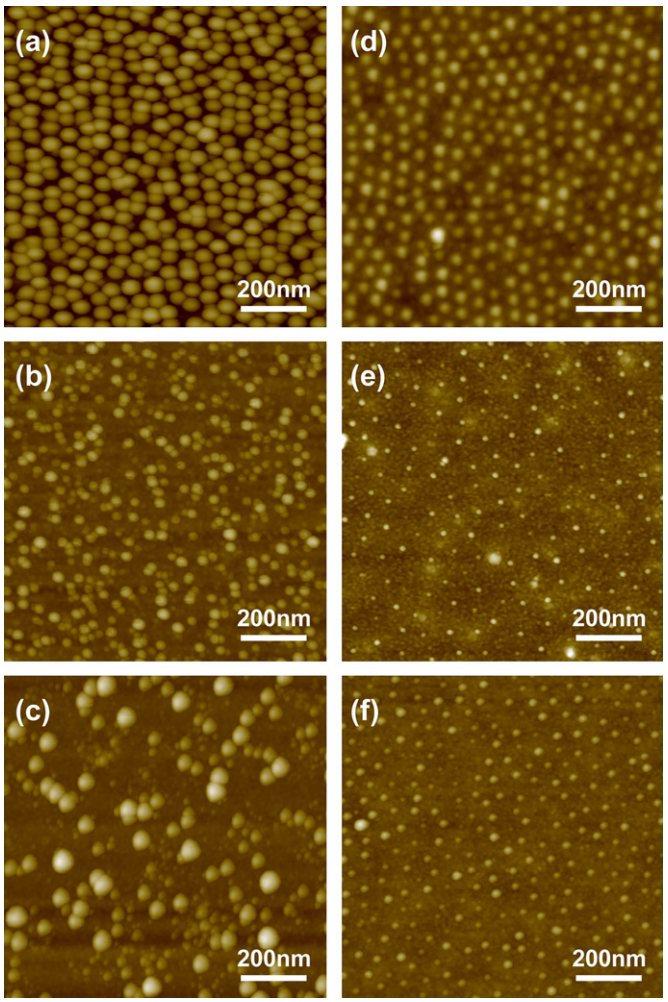

Fig. 1. Tapping mode AFM images of Au nanoparticles prepared by inverse micelle encapsulation using diblock copolymers with different head and tail lengths: (a)–(c) PS(53 000)–P2VP(43 800) (sample #5), (d)–(f) PS(81 000)–P2VP(14 200) (sample #2). Micrographs (a) and (d) were obtained directly after dip-coating; (b) and (e) after in situ polymer removal by annealing in UHV to 623 K (23 h) and 773 K (0.5 h), respectively, and (c) and (f) after five TPD cycles of CO oxidation ($CO(0.6\ L) + O_2(0.3\ L)$ dosing at ~95 K and a maximum TPD temperature of 500 K). The height scales are (a) $z = 45$ nm, (b) $z = 25$ nm, (c) $z = 30$ nm, (d) $z = 15$ nm, (e) $z = 13$ nm, (f) $z = 18$ nm.

concentration ratio). This factor has also an influence over the uniformity of the nanoparticle surface coverage after substrate dip-coating. High r ratios resulted in larger particles less uniformly dispersed over the substrate's surface. Table 1 contains additional information on the molecular weights of the diblock copolymers used in the present study as well as on the relative metal polymer core concentration ratios.

Electron-beam evaporated polycrystalline Ti films (15 nm-thick) evaporated on n-Si(1 1 1) wafers have been used as substrate. Ultrathin TiO_2 films were formed upon substrate exposure to air. Substrate dip-coating into the gold polymeric solution at a speed of 1 μm/min resulted in a monolayer-thick film of monodispersed gold nanoparticles covered by the polymer.

The characterization of the sample morphology (nanoparticle size and substrate distribution) before and after polymer removal as well as after TPD was performed ex situ by AFM in tapping-mode (Digital Instruments, Multimode). The lattice parameter and phase of the Au nanoparticles were characterized by high-resolution transmission electron microscopy (HR-TEM) carried out with an FEI (in the past: Philips) Tecnai F20ST microscope (field emission gun, high tension of 200 kV, Super-Twin lens). As such, the gold nanoparticles were deposited onto amorphous carbon films, which are supported by copper grids (commercial TEM grids).

The ex situ prepared samples were subsequently transferred into an ultrahigh vacuum system (UHV) for polymer removal and electronic/chemical characterization. All in situ investigations were performed in a modular UHV system (SPECS GmbH) specially designed for the preparation and characterization of nanoscaled catalysts. The analysis chamber is equipped with an hemispherical electron energy analyzer (Phoibos 100) and dual-anode (Al-Kα, 1486.6 eV and Ag-Lα, 2984.4 eV) monochromatic X-ray source (XR50, SPECS GmbH) for XPS, and a differentially-pumped quadrupole mass spectrometer (QMS, Hiden Analytical, HAL 301/3F) with an electron-beam sample heating system connected to a PID temperature controller (Eurotherm, 2048) for TPD experiments. The base pressure in this chamber is $1–2 \times 10^{-10}$ mbar.

Polymer removal from the gold nanoparticle surface was achieved in situ (UHV) by annealing. The annealing temperatures of all samples investigated lie above the glass transition temperature of both, PS (381 K) and P2VP

Table 1
Summary of the parameters tuned during the synthesis of size- and shape-selected gold nanoparticles

Sample	PS/P2VP molecular weight (g/mol)	$HAuCl_4$/P2VP ratio	Anneal T (K)/time (h)	Particle height (nm)		Particle diameter (nm)		Interparticle distance (nm)
				AFM	STM	AFM	STM	AFM
#1	81 000/14 200	0.2	773/0.5	1.9 ± 0.5	2.8 ± 0.2	18 ± 3	10.5 ± 0.5	78 ± 12
#2	81 000/14 200	0.6	773/0.5	3.6 ± 0.8	4.3 ± 0.1	16 ± 3	12.8 ± 0.1	76 ± 9
#3	81 000/14 200	0.75	773/0.5	4.0 ± 0.8	–	14 ± 3	–	74 ± 11
#4	8200/8300	0.1	773/0.5	2.1 ± 0.4	1.9 ± 0.1	14 ± 3	7.8 ± 0.2	27 ± 6
#5	53 000/43 800	0.4	623/23	6.1 ± 1.0	–	38 ± 7	–	44 ± 9, 83 ± 17

The optimum annealing conditions (temperature and time) for each polymer type and the respective particle height, diameter, and interparticle distance distributions measured by AFM and STM are given.

(373 K) polymer blocks. Further sample preparation details can be found in Table 1.

The annealing conditions vary depending on the polymer's molecular weight. A systematic study was performed in order to obtain the optimum annealing parameters (temperature and time) that minimize gold agglomeration ensuring nearly complete polymer removal. The evolution of the carbon signal was monitored by XPS to ensure the removal of the polymer from the nanoscaled gold surfaces.

The size-dependent electronic structure of the nanoclusters was investigated in situ by XPS and their reactivity for CO oxidation was monitored by TPD. The XPS spectra were acquired using Al-Kα radiation (1486.6 eV) at a power of 400 W with an electron pass energy of 18 eV. For TPD, the sample was placed in front of a glass-probe differentially pumped QMS with a 5 mm circular aperture. The sample to QMS distance was ~3 mm. The samples were dosed at low temperature (95 K) first with CO and subsequently with O_2 via a manual leak valve that allows the entire chamber to be filled with the dosing gases. Once the sample was positioned in front of the mass spectrometer, the absolute coverage was determined from numerical integration of the TPD spectra. The dosing conditions used in these experiments were 0.6 L for CO and 0.3 L for O_2. In our TPD experiments, the heating rate was automatically controlled, and linear heating ramps were acquired with a rate $\beta = 5.0 \pm 0.1$ K/s. The temperature measurements were carried out with a K-type thermocouple located underneath the sample and spot welded to the sample holder. The error in the temperature measurements was estimated to be less than ±1 K.

3. Results and discussion

3.1. Morphology and crystalline structure (AFM/TEM)

Fig. 1 displays AFM micrographs of gold nanoparticles synthesized by inverse micelle encapsulation using two diblock copolymers with different PS–P2VP molecular ratios (samples #5 (left column) and #2 (right column) in Table 1). The top row ((a) and (d)) presents images of the nanoparticles immediately after dip-coating on polycrystalline TiO_2 surfaces. The images shown in the central row ((b) and (e)) were taken after polymer removal by annealing in UHV (see Table 1 for details on the annealing conditions). The bottom row ((c) and (f)) contains micrographs measured ex situ after five TPD cycles of CO oxidation. Reactive coarsening (Ostwald ripening) is observed for the sample with the largest nanoparticles investigated in this paper (Fig. 1(c), sample #5). The size and substrate distribution of the smaller and more uniformly dispersed nanoparticles in sample #2 remained unaffected by the chemical reaction, Fig. 1(f).

Fig. 2 shows the particle size distributions obtained from the analysis of the AFM images in Fig. 1 taken before (Fig. 2(a) and (c)) and after TPD (Fig. 2(b) and (d)). As mentioned before, for our largest nanoparticles

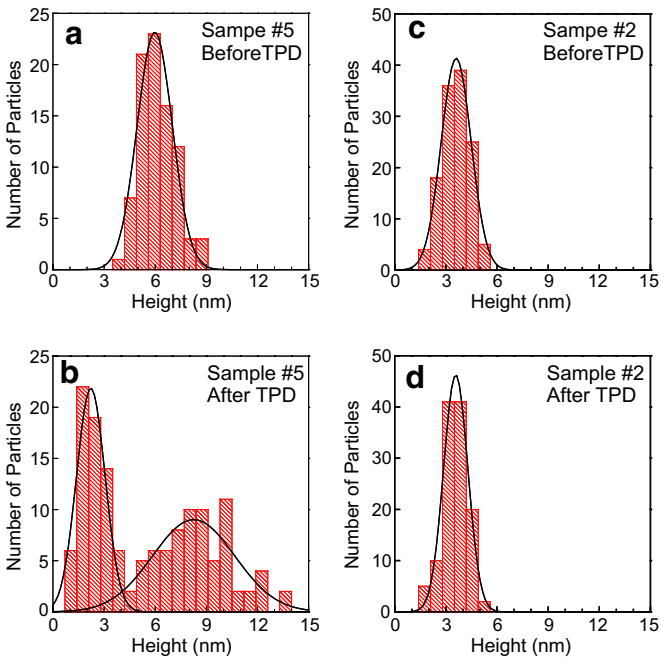

Fig. 2. Size distribution of samples #5 and #2 obtained from AFM images taken at room temperature before (top) and after (bottom) CO oxidation.

(6.1 ± 1.0 nm, sample #5), a bimodal size-distribution with average heights of 2.2 ± 0.6 nm and 8.3 ± 1.7 nm is obtained after TPD, Fig. 2(b). The average height of sample #2 did not change upon gas exposure, Fig. 2(d). This result is in agreement with a previous work by Lai and Goodman [42] that showed size-dependent Ostwald ripening during CO oxidation by UHV evaporated Au nanoclusters deposited on TiO_2(1 1 0).

In order to rule out polymer effects from the catalytic activity of our size-selected nanoparticles, we have also synthesized a second set of samples with three distinct average size distributions obtained using only one diblock copolymer, PS(81 000)/P2VP(14 200), but changing the $HAuCl_4$/P2VP concentration ratios (see samples #1–#3 in Table 1 and Fig. 1(e) as example).

TEM measurements were conducted on samples similarly prepared to #1 and #4, but deposited on C-coated Cu grids. Fig. 3 shows TEM images obtained after polymer removal by annealing in UHV to 773 K. The TEM sample analogous to sample #4 contains the smallest particles studied in this work. From the bright-field image in Fig. 3(a), a lattice plane spacing of $d_{111} = 0.244 \pm 0.017$ nm of the 8 nm sized Au nanoparticle was measured and a lattice parameter of $a = 0.423 \pm 0.03$ nm of the fcc phase was determined. A detailed fast Fourier transform (FFT) pattern analysis of the 15-nm-sized polycrystalline Au particle (sample #1) obtained from the bright-field image in Fig. 3(b) revealed the fcc phase with a lattice plane spacing of $d_{200} = 0.213$ nm and a lattice constant of $a = 0.428 \pm 0.021$ nm. In both samples, the nanoparticles were found to be polycrystalline and multifaceted.

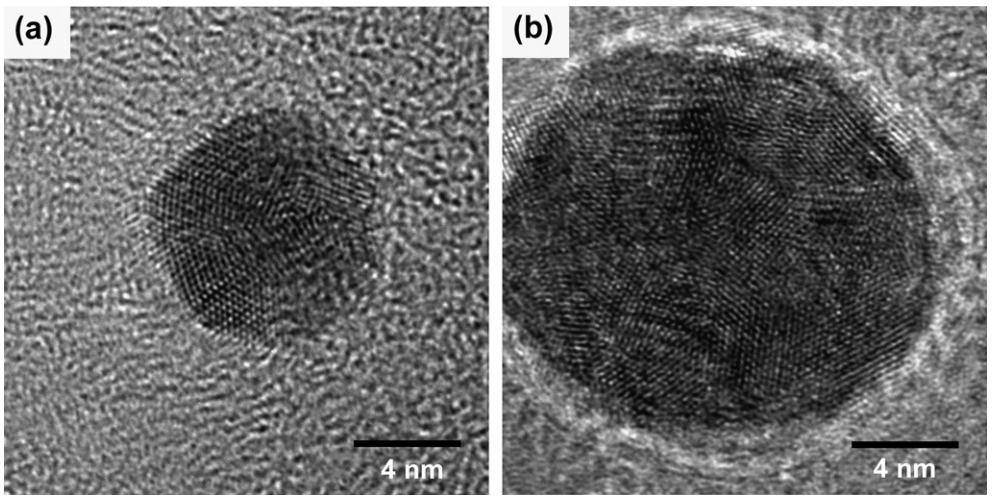

Fig. 3. TEM images (a) and (b) obtained from samples #4 and #1, respectively, after in situ polymer removal by annealing in UHV (773 K/0.5 h).

Previous cross sectional TEM work conducted by Kastle et al. [40] on similarly synthesized nanoparticles but after polymer removal by O_2 or H_2 plasma treatments provided evidence for the spherical shape of these types of nanoparticles. However, recent STM results from our group [43] showed that the shape of the nanoparticles is altered during the high-temperature UHV annealing (773 K) treatment employed here to remove the encapsulating polymer, resulting in "pancake-like" hemispherical nanoparticles. A good agreement between the nanoparticle heights determined by AFM and STM was found. As expected, the apparent lateral size of the particles measured by AFM was larger than the one measured by STM and TEM due to the large curvature radius of the AFM tip (~7 nm).

3.2. Electronic and chemical structure (XPS)

XPS was used to monitor changes in the chemical composition of the nanoparticle/metal-oxide support after UHV annealing. Fig. 4 shows XPS spectra from the Au-4f core level region before (curves i, iii, and v) and after (curves ii, iv, and vi) annealing in vacuum (samples #3–#5). The binding energy (BE) scale displayed has been calibrated using the Ti-2p XPS peaks as reference.

Before annealing, two XPS doublets with maxima at (84.0 and 87.7 eV) and (85.5–85.7 and 89.1–89.4 eV) were observed for samples #3 and #5, Fig. 4 (curves iii and v). Sample #4, however, only showed the second doublet. The first doublet, accounting for approximately 25% and 16% of the total spectral area measured for samples #3 and #5, respectively, is assigned to Au^0 ($4f_{7/2}$ and $4f_{5/2}$ peaks). According to Glass et al. [44], the second doublet at 85.7 eV and 89.5 eV corresponds to Au^{3+} in $AuCl_4^-$. Interestingly, our measurements showed that Au^{3+} is more stable on the smallest nanoparticles (sample #4), since no Au^0 signal from the spontaneous decomposition of Au^{3+} was detected before the thermal treatment. Further, the slightly different BE shifts observed for the Au^{3+} doublet in the three different samples can be attributed to nanoparticle charging due to the insulating encapsulating polymer, as well as to the distinct internal structure of the as-prepared nanoclusters inside the micelles [44]. Previous TEM work

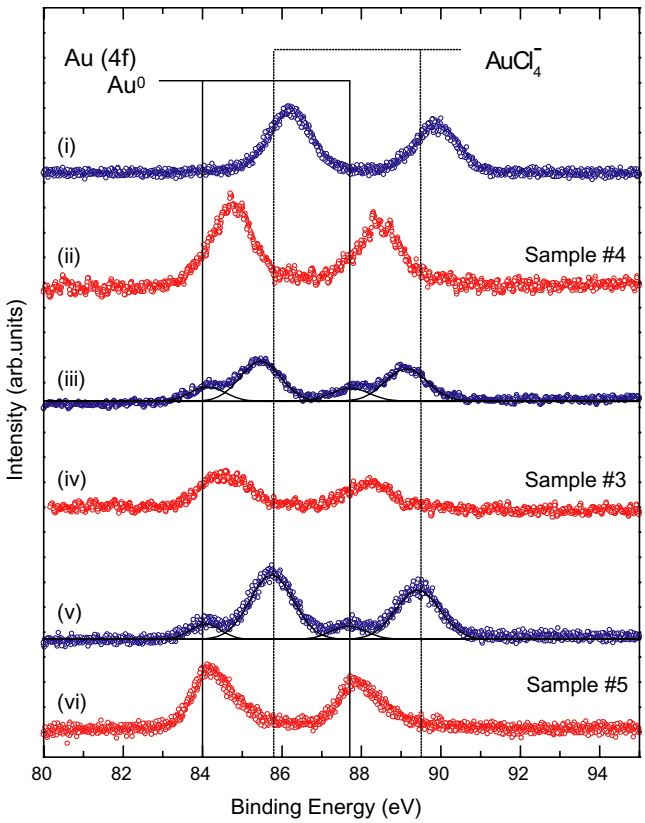

Fig. 4. XPS spectra (Al-Kα = 1486.6 eV) corresponding to the Au-4f core level of Au nanoparticles supported on TiO_2/Ti(15 nm) and measured at RT before (curves i, iii, and v) and after (curves ii, iv, and vi) annealing in UHV. The spectra correspond to nanoparticles synthesized by encapsulation on three diblock copolymers with distinct core and tail lengths (see Table 1): sample #4 (curves i and ii), #3 (curves iii and iv), and #5 (curves v and vi).

on similarly prepared samples [7,8,40,44] revealed the existence of small cluster domains within each polymeric cage.

After in situ annealing, Fig. 4 (curves ii, iv, and vi), only one doublet at a binding energy of 84.5 ± 0.3 eV is observed for samples #3–#5. This result indicates the complete reduction of Au^{3+} complexes to Au^0. As previously reported, the measured binding energies are slightly larger than the ones corresponding to bulk Au^0 (vertical solid line, 84 and 87.7 eV) [7]. Such well known positive BE shifts typical of small nanoparticles are attributed to changes in the electronic structure of clusters with decreasing size (initial state effects) [45,46], as well as to positive charge left on the cluster surface during the photoemission process (final state effects) [7,47]. This effect is illustrated in Fig. 5, where the Au^0-$4f_{7/2}$ binding energies measured after annealing have been displayed as a function of cluster height. The largest shift, +0.8 eV, was observed for the smallest nanoparticles investigated, sample #4, Fig. 4 (curve ii). This result is in agreement with our AFM data (1.9 ± 0.5 nm cluster height). A BE close to bulk gold was measured for sample #5 (Fig. 4 (curve vi)) for which the cluster height measured by AFM was 6.1 ± 1.0 nm.

Special attention has been dedicated to monitor any residual chlorine signal using XPS, since Cl/Au molar ratios as low as 0.0006 were found to have a poisonous effect in CO oxidation reactions [48–50]. No detectable amounts of either N-1s (399.3 eV) [51] or Cl-2s (270.0 eV) [27] from the P2VP [–$CH_2CH(C_5H_4N)$–]n and $HAuCl_4$ salt, respectively, were measured by XPS after annealing.

Fig. 6(a) displays XPS Ti-2p spectra from an Au-covered Ti(15 nm)/Si(1 1 1) substrate (sample #1) before and after in situ annealing. XPS peaks characteristic of Ti^0 (454 and 460 eV) and Ti^{4+} in TiO_2 (459 and 464.7 eV) were observed before annealing (Fig. 6(a) (curve i)), in agreement with previous literature reports [52]. After annealing to 773 K, a significant binding energy shift attributed to the formation of TiC (454.5 eV and 460.5 eV) was observed (Fig. 6(a) (curve ii)). The peak position measured for carbon after annealing, Fig. 6(b) (curve ii), is also in agreement with C-1s in TiC (281.8 eV) [53,54]. This result provides evidence for a temperature-driven reaction between Ti and C. Further quantitative analysis integrating the Ti-2p and C-1s peaks indicate that the TiC thin film has 1:1 titanium to carbon surface stoichiometry. According to that, all annealed gold samples investigated in this article are supported on carbon passivated titanium films.

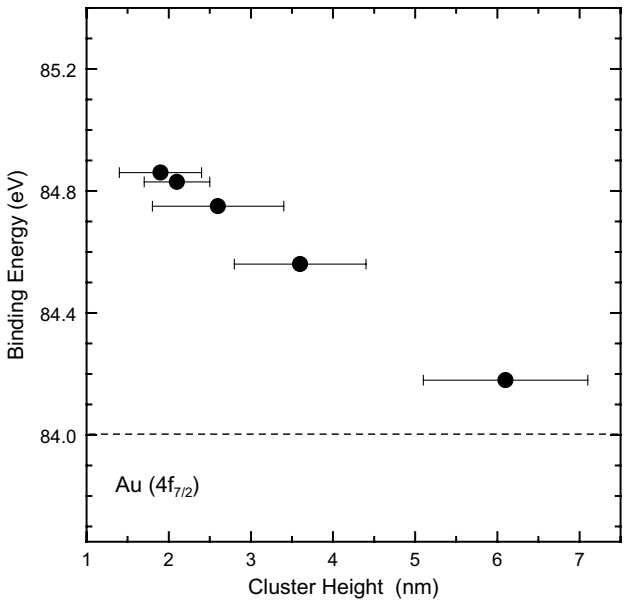

Fig. 5. Binding energy versus cluster height on TiC substrate obtained from XPS Au^0-$4f_{7/2}$ spectra. Different cluster sizes were obtained by using encapsulating PS–P2VP polymers with distinct molecular weights and by modifying the relative gold/polymer concentration. (See Table 1 for further details on the sample preparation.)

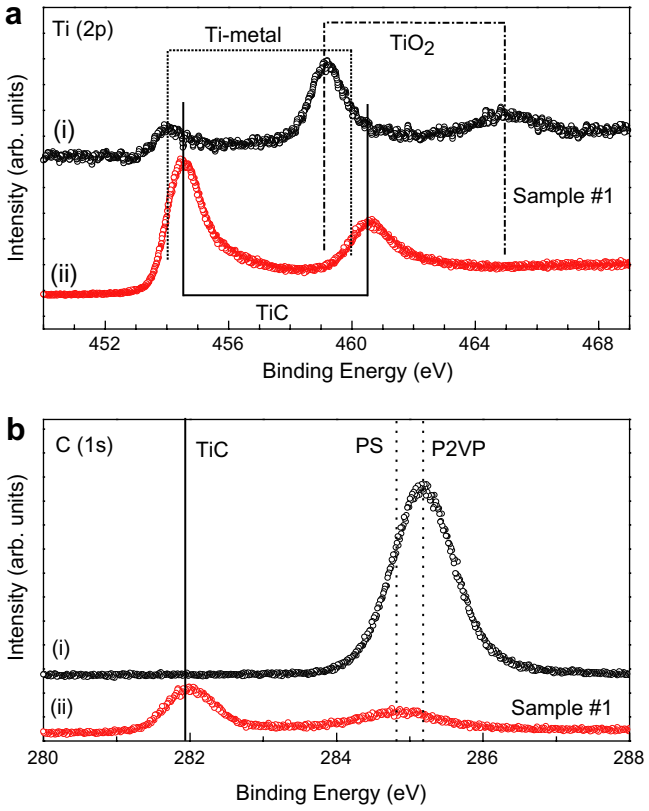

Fig. 6. XPS spectra of (a) Ti-2p and (b) C-1s core levels measured from sample #1 before (curve i) and after (curve ii) annealing in UHV (773 K/0.5 h).

The XPS results indicate a stronger interaction of C with Ti than with Au, and the formation of gold carbide is excluded in agreement with previous report [55,56]. The same amount of residual carbon was observed in all samples after the different annealing treatments. The relative carbon concentration after/before annealing is calculated to be less than 10%. This signal intensity was also comparable to the one measured on a gold and polymer free TiO_2/Ti(15 nm)/Si(1 1 1) substrate after annealing in UHV in the presence of adventitious carbon.

3.3. Chemical reactivity (TPD)

3.3.1. TiC support

The catalytic activity of TiC thin films for CO oxidation was characterized using TPD. Fig. 7 shows CO_2 desorption signals measured on TiO_2/Ti(15 nm) substrates coated with gold-free polymeric solutions. These samples were subsequently annealed in UHV to 773 K for 30 min. TPD graphs corresponding to TiO_2/Ti(15 nm) substrates coated with PS(81 000)-*b*-P2VP(14 200) (same polymer used during the synthesis of samples #1–#3) and PS(8200)-*b*-P2VP(8300) (used in the synthesis of sample #4), are displayed in Fig. 7(a) and (b), respectively. Upon exposing the samples to 0.6 L of CO and 0.3 L of O_2, two desorption features named σ_1 and σ_2 states were observed. TPD peaks at 143 K and 410 K, were measured for PS(81 000)-*b*-P2VP(14 200), Fig. 7(a) (open circles). Similar desorption temperatures (145 K and 470 K) were also measured for the PS(8200)-*b*-P2VP(8300)-coated TiO_2/Ti(15 nm) sample. From the integration of the CO_2 desorption graphs, a probability for CO to CO_2 conversion ($P_{CO_2/CO}[\sigma_1+\sigma_2]$) [57] of approximately 0.02 was found for both samples. If only the low-temperature desorption feature (σ_1 state) is taken into consideration, a 0.001 conversion was obtained. Thus, our data show that the polycrystalline TiC films formed on these samples upon UHV annealing are poor catalysts for low as well as for high-temperature CO oxidation. No CO_2 desorption peaks were observed for either sample before gas dosing, Fig. 7 (solid circles).

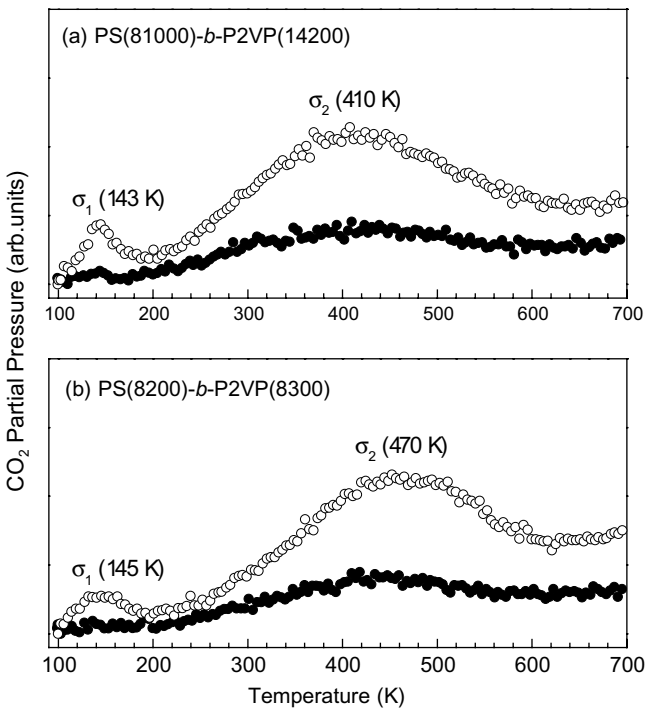

Fig. 7. CO_2 TPD spectra on a TiC substrate synthesized by dip-coating a TiO_2/Ti(15 nm) thin film with (a) PS(81 000)-*b*-P2VP(14 200) and (b) PS(8200)-*b*-P2VP(8300) polymers and following annealing in UHV to 773 K for 30 min. CO_2 TPD signals were measured before gas exposure (●) and after sample dosing at ~95 K first with 0.6 L of CO and subsequently with 0.3 L of O_2 (○). A linear heating ramp with $\beta = 5$ K/s was used. Two desorption features σ_1 and σ_2 are observed.

3.3.2. Au-nanoparticles/TiC

Fig. 8 displays CO_2 desorption spectra obtained during the low-temperature oxidation of CO over size-selected gold nanoparticles supported on TiC. The data in Fig. 8(a) correspond to samples with the same interparticle distance but different size (samples #1–#3) synthesized using PS(81 000)–P2VP(14 200) micelles with different metal/polymer concentration ratios. In Fig. 8(b), desorption data from samples containing nanoparticles with two distinct average size and interparticle distance distributions synthesized using two different encapsulating polymers (sample #4, PS(8200)–P2VP(8300) and sample #5 PS(53 000)–P2VP(43 800)) are shown.

Fig. 8(a) shows a clear size-dependence of the low-temperature catalytic oxidation of CO on TiC supported Au nanoparticles. The smallest nanoparticles investigated (sample #1) show two CO_2 desorption states (named γ and π in the following text) at temperatures of 115 K and 150 K, respectively. With increasing particle size (samples #2 and #3), a shift towards higher CO_2 desorption temperatures is observed, and both samples show γ and π states at 138 K and 193 K, respectively.

In agreement with previous studies on supported gold nanoparticles [4,14,58], we assign the first desorption feature, γ, to CO adsorption and oxidation on the surface of the gold nanoparticles (kinks and steps). Since no significant change in the width of the nanoparticle size distributions is observed by comparing sample #1 with #2 and #3, the broadening of the desorption peaks observed for samples #2 and #3 may be attributed to the distinct nanoparticle-faceting measured by TEM for different cluster sizes. Previous experimental and theoretical works show an enhanced chemical activity for stepped Au(2 1 1) [14] and Au(3 3 2) [59] surfaces as compared to smooth Au(1 1 1) surfaces. DFT Calculations by Mills et al. [18] demonstrated that the roughness of the surface, i.e., the presence of highly uncoordinated atoms, is important for the dissociation of O_2. Additional DFT studies by Mavrikakis et al. [14,60] correlated the enhanced chemical activity of small gold nanoparticles to the high density of step-sites as well as to size-dependent surface-strain.

The second state, π, is attributed to CO oxidation occurring at the perimeter of the gold nanoparticles; i.e., at the interface between the gold nanoparticle and the TiC substrate. Earlier theoretical investigations on Au clusters supported on TiO_2(1 1 0) [61] and MgO(1 0 0) [62] revealed that special active sites favorable for CO oxidation are available at the nanoparticle/metal-oxide support interface. Liu's work [61] indicated that the role of the metal-oxides support is to promote the transfer of charge from Au to O_2 by lowering the 2π energy level of the molecule. Interestingly, no direct charge transfer from the substrate to the molecule was observed. Ionic-like bonding is reported by the authors

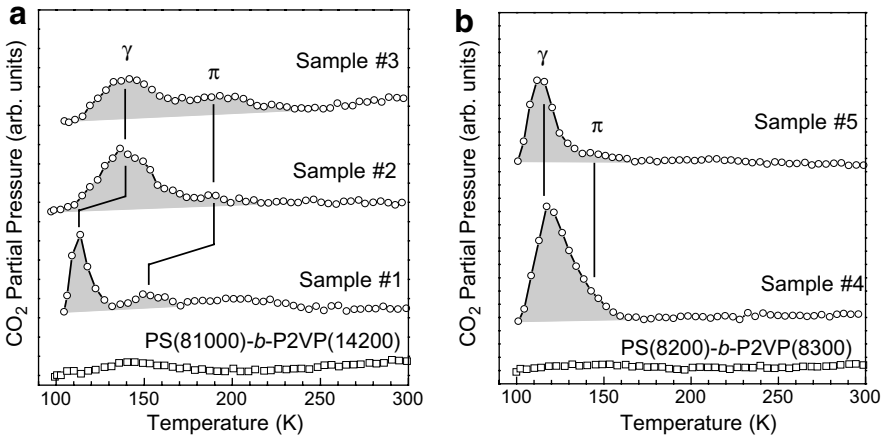

Fig. 8. CO_2TPD spectra from samples #1–#5 (see Table 1 for details) and two TiC substrates prepared by annealing two TiO_2/Ti(15 nm) films coated with PS(81 000)–P2VP(14 200) (a) and PS(8200)–P2VP(8300) (b) to 773 K. The samples were dosed with 0.6 L of CO and 0.3 L of O_2 at ~95 K, and a linear heating ramp of $\beta = 5$ K/s was used. The residual gas background obtained for each sample from desorption spectra measured before sample exposure to the $CO + O_2$ mixture was subtracted. TPD spectra from samples with different average size distributions but identical interparticle distances (a) and both, distinct size and interparticle distance (b) are shown. The area under the peak is highlighted indicating the integration region taken in the subsequent quantitative activity analysis (see text).

representing a highly activated O_2 adsorption state for subsequent CO oxidation. Additional theoretical and experimental work on TiC is needed in order to find out if a similar mechanism is responsible for the enhanced catalytic properties of the Au-nanoparticle/TiC support interface.

Fig. 8(b) shows TPD spectra from gold nanoparticles with different sizes (samples #4 and #5) that were synthesized using two distinct diblock-copolymers PS(8200)–P2VP(8300) and PS(53 000)–P2VP(43 800) (see Table 1 for details). These polymers have shorter tail-lengths than the polymer employed in the preparation of the samples shown in Fig. 8(a), and therefore, the interparticle distance is now smaller.

The TPD spectrum from sample #4 (average height 2.1 ± 0.4 nm) shows a state at 118 K (γ) and a shoulder at 146 K (π state). The AFM images from this sample (not shown) indicate that most of the surface of the TiC support is covered with gold nanoparticles, with an interparticle distance of about 27 nm. The TPD spectrum from our largest nanoparticles (height $= 6.1 \pm 1.0$ nm), sample #5, also shows similar desorption features at 113 K and 146 K, respectively. At first glance, this result seems to contradict our previous observation, Fig. 8(a), where higher desorption temperatures were obtained for larger nanoparticle sizes. However, the inconsistency disappears if one considers the changes in size that these nanoparticles experienced upon gas exposure (see sample #5 in Fig. 1(c) for details). Our AFM images revealed that reactive coarsening (Ostwald ripening) occurs for the samples where the interparticle distance is small (samples #4 and #5), while the size and substrate arrangement of the more widely spaced nanoparticles (samples #1–#3) did not seem to be affected. This is not a temperature-driven effect, since the same samples were previously annealed to a higher temperature (773 K) than our maximum TPD temperature (500 K) and no agglomeration was observed by AFM (Fig. 1(b), sample #5). Our results provide evidence for interparticle interaction in the presence of $CO + O_2$. For sample #5, Fig. 2(b), after the reaction, bimodal size distributions with smaller (~2.2 nm) and larger (~8.3 nm) particle sizes than the analogous non-exposed sample (~6.1 nm) were obtained.

Similar behavior was observed for sample #4 (not shown) with a bimodal size distribution of ~1.5 nm and ~3.2 nm after gas exposure. In both cases, only the small clusters formed (~2.2 nm for sample #5) are considered to contribute to the production of CO_2. Our results are broadly consistent with a previous investigation by Lai et al. showing Ostwald ripening when Au clusters supported on TiO_2 were exposed at RT to $CO + O_2$ mixtures (2:1, 10 Torr of CO) for 2 h [42].

For the quantitative comparative analysis of the TPD spectra measured on different samples, special care was taken to monitor and keep constant the level of residual water during the different experiments. Date and Haruta [63] reported that ~0.1 ppm of H_2O enhances the catalytic activity at RT more than one order of magnitude. However, a higher concentration of moisture, 6000 ppm, reduced the reaction rate. As pointed out by Kung et al. [64], this factor might be responsible for the discrepancies in the CO oxidation activities observed by various research groups.

Fig. 9 shows the calculated activity for CO_2 production obtained from TPD spectra shown in Fig. 8. The activity was quantified by integrating the CO_2 desorption peaks and normalizing by the total gold surface area (assuming oblate half-ellipsoidal nanoparticle shape) measured by AFM (triangles) and STM (circles). An initial TPD run where the samples were annealed without previous gas exposure was used for background subtraction. Our AFM images confirmed that the first TPD run before gas exposure did not change the morphology of our samples,

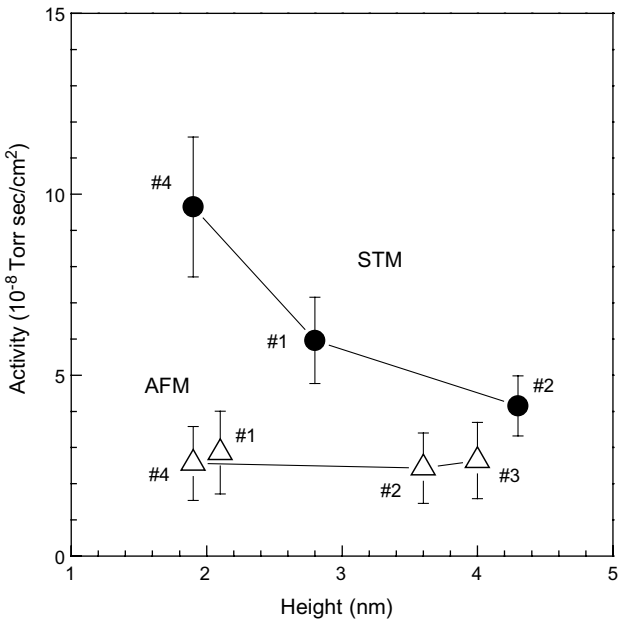

Fig. 9. Normalized catalytic activity of Au nanoparticles for low-temperature CO oxidation displayed as a function of the average nanoparticle size. The total gold surface area has been used in the normalization. The nanoparticle shape has been obtained by using a half-ellipsoid model (pancake-like particle) with average height and diameter obtained by AFM (△) and STM (●). The numbers (#1–#5) displayed near each data point indicate the sample investigated (see Table 1 for details).

since annealing temperatures lower than the ones used for the in situ polymer removal were always used.

Different normalized activity values are obtained when comparing particle dimensions obtained by AFM and STM due to tip-sample convolution effects in AFM that lead to an overestimation of the particle's lateral dimensions and therefore of the total gold surface area.

In agreement to previous observations [7,8,15,42,65,66], our results show a size-dependence in the catalytic activity of gold nanoparticles for low-temperature CO oxidation, with the smallest nanoparticles considered displaying the highest activities. It is important to point out that the diameter of the smallest nanoparticles investigated here (~7.8 nm, STM) is significantly larger than the sizes investigated by Goodman and Haruta's groups (~3.5 nm). Previous experiments conducted by Chou et al. [67] at atmospheric pressure (mass flow reactor) on similarly prepared 8-nm-large Au nanoparticles supported on nanocrystalline TiO_2 powder also showed a significant activity for CO oxidation. We attribute the enhanced catalytic activity of our relatively large pancake-shaped nanoparticles to the large nanoparticle/support contact area [5]. This is in agreement with a report by Pietron et al. [68] that ascribed the high activity of relatively large (6 nm) gold nanoparticles in Au–TiO_2 composite aerogels to the large nanoparticle-support contact area obtained using this synthesis route [68]. However, a recent experimental work conducted in Goodman's group suggested that it is not the Au-support interface but rather the Au morphology that is the critical parameter responsible for the high catalytic activity observed for CO oxidation. In particular, their experiments demonstrated that a monolayer structure, in direct contact with the TiO_x substrate, was more than an order of magnitude less active than a similarly prepared bi-layer structure [13,17]. A theoretical work from Norskov's group predicted that such an Au-only reaction is energetically competitive with other pathways involving the metal-oxide support [69].

Our studies clearly show a size-dependence of the reactivity of size-selected inverse micelle-encapsulated gold nanoparticles, with the smallest nanoparticles displaying the highest activities. Further work will be required in order to get insight on whether it is the nanoparticle diameter and particle-substrate contact area or just the particle height as the main parameter that should be tuned in order to obtain increased reactivities.

4. Conclusions

Size-selected Au nanoparticles synthesized by diblock copolymer encapsulation and supported on ultrathin TiC films were used as model system to in situ investigate the size-reactivity relationship. Our XPS data show a monotonic increase of the gold binding energy with decreasing nanoparticle size, with a maximum shift of +0.8 eV for the ~2-nm-high particles. This result correlates with the enhanced catalytic activity for low-temperature CO oxidation measured by TPD for the smallest nanoparticles. Two different desorption sites were identified and attributed to CO_2 production at steps/kinks in the gold surface as well as the Au–TiC interface.

AFM images acquired before and after the chemical reaction (TPD) showed that even in the presence of low gas dosings, the gold nanoparticles undergo morphological/structural changes that have a significant impact on their catalytic performance. It must be noted that those changes were not observed when the nanocatalysts underwent annealing alone in UHV to similar temperatures. In addition, our experimental results show that interparticle interactions may affect the lifetime of the catalysts. Widely spaced nanoparticles (~80 nm interparticle distance) showed no deactivation after several TPD cycles. However, more densely distributed particles (~30 nm) experienced Ostwald ripening and a fast deactivation profile.

Acknowledgments

Work financially supported by the National Science Foundation (NSF-CAREER award, 0448491) and ACS-Petroleum Research Foundation (PRF-G award, 42701-G5) and the Deutsche Forschungsgemeinschaft (Sonderforschungsbereich SFB 445).

References

[1] J. Schwank, Gold Bull. 16 (1983) 103.
[2] P.A. Sermon, G.C. Bond, P.B. Wells, J. Chem. Soc., Faraday Trans. 1 75 (1979) 385.
[3] M. Haruta, T. Kobayashi, H. Sano, N. Yamada, Chem. Lett. (1987) 405.
[4] M. Haruta, Catal. Today 36 (1997) 153.
[5] M. Haruta, J. New Mater. Electrochem. Syst. 7 (2004) 163.
[6] M. Valden, X. Lai, D.W. Goodman, Science 281 (1998) 1647.
[7] B. Roldan Cuenya, S.H. Baeck, T.F. Jaramillo, E.W. McFarland, J. Am. Chem. Soc. 125 (2003) 12929.
[8] T.F. Jaramillo, S.H. Baeck, B. Roldan Cuenya, E.W. McFarland, J. Am. Chem. Soc. 125 (2003) 7148.
[9] C.T. Campbell, S.C. Parker, D.E. Starr, Science 298 (2002) 811.
[10] S.K. Shaikhutdinov, R. Meyer, M. Naschitzki, M. Baumer, H.J. Freund, Catal. Lett. 86 (2003) 211.
[11] U. Diebold, Surf. Sci. 578 (2005) 1.
[12] A. Cho, Science 299 (2003) 1684.
[13] T.V. Choudhary, D.W. Goodman, Appl. Catal., A 291 (2005) 32.
[14] M. Mavrikakis, P. Stoltze, J. Norskov, Catal. Lett. 64 (2000) 101.
[15] N. Lopez, T.V.W. Janssens, B.S. Clausen, Y. Xu, M. Mavrikakis, T. Bligaard, J.K. Norskov, J. Catal. 223 (2004) 232.
[16] M. Valden, S. Pak, X. Lai, D.W. Goodman, Catal. Lett. 56 (1998) 7.
[17] M.S. Chen, D.W. Goodman, Catal. Today 111 (2006) 22.
[18] G. Mills, M.S. Gordon, H. Metiu, J. Chem. Phys. 118 (2003) 4198.
[19] C. Lemire, R. Meyer, S. Shaikhutdinov, H.J. Freund, Angew. Chem., Int. Ed. 43 (2004) 118.
[20] M. Mavrikakis, B. Hammer, J.K. Norskov, Phys. Rev. Lett. 81 (1998) 2819.
[21] J.Z. Xu, P. Henriksen, J.T. Yates, J. Chem. Phys. 97 (1992) 5250.
[22] J.Z. Xu, J.T. Yates, J. Chem. Phys. 99 (1993) 725.
[23] G.A. Somorjai, K.R. McCrea, J. Zhu, Top. Catal. 18 (2002) 157.
[24] G.A. Somorjai, Chem. Rev. 96 (1996) 1223.
[25] S. Mori, Y. Shitara, Appl. Surf. Sci. 78 (1994) 269.
[26] H. Hakkinen, W. Abbet, A. Sanchez, U. Heiz, U. Landman, Angew. Chem., Int. Ed. 42 (2003) 1297.
[27] H.G. Boyen et al., Science 297 (2002) 1533.
[28] J.M.C. Soares, P. Morall, A. Crossley, P. Harris, M. Bowker, J. Catal. 219 (2003) 17.
[29] S. Chretien, H. Metiu, Catal. Lett. 107 (2006) 143.
[30] L. Leclercq, M. Provost, H. Pastor, J. Grimblot, A.M. Hardy, L. Gengembre, et al., J. Catal. 117 (1989) 371.
[31] L. Leclercq, M. Provost, H. Pastor, G. Leclercq, J. Catal. 117 (1989) 384.
[32] R.B. Levy, M. Boudart, Science 181 (1973) 547.
[33] J.H. Sinfelt, D.J.C. Yates, Nat. Phys. Sci. 229 (1971) 27.
[34] P. Liu, J.A. Rodriguez, J.T. Muckerman, J. Mol. Catal. A: Chem. 239 (2005) 116.
[35] Z.Y. Chen, S.S. Perry, A. Savan, P.M. Adams, S.V. Didziulis, J. Vac. Sci. Technol. A 23 (2005) 234.
[36] R.L. Guenard, L.C. Fernandez-Torres, B.I. Kim, S.S. Perry, P. Frantz, S.V. Didziulis, Surf. Sci. 515 (2002) 103.
[37] P. Frantz, S.V. Didziulis, L.C. Fernandez-Torres, R.L. Guenard, S.S. Perry, J. Phys. Chem. B 106 (2002) 6456.
[38] I. Kojima, E. Miyazaki, J. Catal. 89 (1984) 168.
[39] M. Orita, I. Kojima, E. Miyazaki, Bull. Chem. Soc. Jpn. 59 (1986) 689.
[40] G. Kastle et al., Adv. Funct. Mater. 13 (2003) 853.
[41] J.P. Spatz, S. Mossmer, C. Hartmann, M. Moller, T. Herzog, M. Krieger, H.G. Boyen, P. Ziemann, B. Kabius, Langmuir 16 (2000) 407.
[42] X.F. Lai, D.W. Goodman, J. Mol. Catal. A: Chem. 162 (2000) 33.
[43] A. Naitabdi, L.K. Ono, B. Roldan Cuenya, Appl. Phys. Lett. 89 (2006) 043101.
[44] R. Glass, M. Arnold, J. Blummel, A. Kuller, M. Moller, J.P. Spatz, Adv. Funct. Mater. 13 (2003) 569.
[45] P. Zhang, T.K. Sham, Phys. Rev. Lett. 90 (2003) 245502.
[46] M.G. Mason, Phys. Rev. B 27 (1983) 748.
[47] G.K. Wertheim, S.B. DiCenzo, S.E. Youngquist, Phys. Rev. Lett. 51 (1983) 2310.
[48] P. Broqvist, L.M. Molina, H. Gronbeck, B. Hammer, J. Catal. 227 (2004) 217.
[49] H.S. Oh, J.H. Yang, C.K. Costello, Y.M. Wang, S.R. Bare, H.H. Kung, M.C. Kung, J. Catal. 210 (2002) 375.
[50] H.H. Kung, M.C. Kung, C.K. Costello, J. Catal. 216 (2003) 425.
[51] G. Beamson, D. Briggs (Eds.), High Resolution XPS of Organic Polymers – The Scienta ESCA300 Database, John Wiley & Sons, New York, 1992.
[52] J.F. Moulder, W.F. Stickle, P.E. Sobol, K.D. Bomben (Eds.), Handbook of X-ray Photoelectron Spectroscopy, Perkin–Elmer, Physical Electronics, Inc., Eden Praire (MN), 1995.
[53] V. Benavides, E. Restrepo, A. Devia, Phys. Status Solidi C 2 (2005) 3770.
[54] T. Tachibana, B.E. Williams, J.T. Glass, Phys. Rev. B 45 (1992) 11975.
[55] T. Tachibana, B.E. Williams, J.T. Glass, Phys. Rev. B 45 (1992) 11968.
[56] Y. Wang, X. Liu, C. Zhen, H. Gong, Z. Yan, Y. Yang, S. Ma, Surf. Interface Anal. 29 (2000) 478.
[57] J.M. Gottfried, K.J. Schmidt, S.L.M. Schroeder, K. Christmann, Surf. Sci. 525 (2003) 197.
[58] B. Yoon, H. Hakkinen, U. Landman, A.S. Worz, J.M. Antonietti, S. Abbet, K. Judai, U. Heiz, Science 307 (2005) 403.
[59] C. Ruggiero, P. Hollins, Surf. Sci. 377 (1997) 583.
[60] Y. Xu, M. Mavrikakis, J. Phys. Chem. B 107 (2003) 9298.
[61] Z.P. Liu, X.Q. Gong, J. Kohanoff, C. Sanchez, P. Hu, Phys. Rev. Lett. 91 (2003).
[62] L.M. Molina, B. Hammer, Phys. Rev. Lett. 90 (2003) 206102.
[63] M. Date, M. Haruta, J. Catal. 201 (2001) 221.
[64] M.C. Kung, C.K. Costello, H.H. Kung, Catalysis 17 (2004) 152.
[65] R. Meyer, C. Lemire, S.K. Shaikhutdinov, H.J. Freund, Gold Bull. 37 (2004) 72.
[66] M. Haruta, Chem. Rec. 3 (2003) 75.
[67] J. Chou, N.R. Franklin, S.H. Baeck, T.F. Jaramillo, E.W. McFarland, Catal. Lett. 95 (2004) 107.
[68] J.J. Pietron, R.M. Stroud, D.R. Rolison, Nano Lett. 2 (2002) 545.
[69] I.N. Remediakis, N. Lopez, J.K. Norskov, Angew. Chem., Int. Ed. 44 (2005) 1824.